JOURNAL OF AIRCRAFT
Vol. 40, No. 2, March–April 2003

Blunt Body in Hypersonic Electromagnetic Flow Field

J. S. Shang* and J. Hayes†
U.S. Air Force Research Laboratory, Wright–Patterson Air Force Base, Ohio 45433-7913
J. Menart‡
Wright State University, Dayton, Ohio 45435
and
J. Miller§
U.S. Air Force Research Laboratory, Wright–Patterson Air Force Base, Ohio 45433-7913

A combined experimental and computational effort has been devoted to investigate the interaction of a plasma counterflow jet and magnetoaerodynamic blunt-body phenomenon in hypersonic streams. The weakly ionized, counterflow jet generated by a plasma torch has a vibrionic temperature of 4400 K, an electron temperature around 20,000 K, and electron number density greater than $3 \times 10^{12}/\mathrm{cm}^3$. At a fixed injection stagnation pressure, the plasma injection actually increases drag above that of the room-temperature air counterpart due to a decreased mass flow rate at the elevated temperature. However, at the identical mass flow rate, the plasma injection reveals a greater drag reduction than the room-temperature air jet. It was found that the drag reduction is mostly derived from the viscous–inviscid interaction of the counterflow jet and thermal energy deposition. For the magnetoaerodynamic blunt-body experiment, the electromagnetic effect by an applied magnetic field from the blunt body is detectable, but its quantification remains elusive.

Nomenclature

B = magnetic flux density
D = total drag
E = electrical field strength
J = electric current density
p = pressure
r = radius of hemispheric nose
S = interaction parameter, $\sigma B^2 r/\rho u$
T = temperature
U = conservative variables
ρ = air density
σ = electrical conductivity

I. Introduction

A PROMISING mechanism for improving aerodynamic performance can be derived from electromagnetic force.[1–3] The most effective performance improvement using electromagnetism has been demonstrated via the modified Rankine–Hugoniot condition across a shock. In that, the Joule heating and the work done by the Lorentz force on gas particles have been illustrated as additional entropy alteration mechanisms.[4–6] However, the possibility of reducing the entropy jump, thus, the wave drag, depends on the polarity of an applied magnetic field, the electrical conductivity of the fluid medium, and the interaction of the aerodynamic and electromagnetic force. In a hypersonic stream, the air frequently attains a weakly ionized state, and desired interaction is achievable by applying a magnetic field. The relative importance of aerodynamic and electromagnetic force is measured by the magnetic interaction parameter $S = \sigma B^2 L/\rho u$ (Ref 1). The applied magnetic field strength B and the electrical conductivity of the weakly ionized air σ dominate the interaction.

The first significant magnetoaerodynamic interacting phenomenon was demonstrated by the pioneering work of Ziemer.[7] He has shown the shock standoff distance over a blunt body increased drastically by a factor of 7.5 for an interaction parameter of 69. In his experimental effort, the aerodynamic force was not measured. However, earlier theoretical studies by Bush[8] and Meyer[9] have shown that the interacting force of the electrically conducting fluid with an applied magnetic field and surface heat transfer can produce appreciable changes in hypersonic flow about the blunt body.

A group of experiments using plasma injection from the stagnation region of a blunt body reported an astonishing amount of drag reduction.[10] Although the applied magnetic field was conspicuously absent from these experiments, the counterflow jet interaction, electromagnetic forces, and nonequilibrium thermodynamics were considered as possible key contributing mechanisms for aerodynamic drag reduction via plasma injection. In more recent research efforts by Shang et al.,[11,12] a major portion of the observed wave drag reduction was shown as the consequence of the counterflow jet and bow shock wave interaction. The drag reduction from aerodynamic interaction is realized by altering a single bow shock to a multiple-shock structure by the counterflow jet. In gist, the flowfield consists of the counterflow jet issuing from the stagnation region and reversing its direction downstream by the Mach disk as a free shear layer. A part of the jet stream is entrained to form a toroidal recirculation zone beneath the dividing stream surface. The rest flows over the recirculation zone to become a free shear. As the free shear layer reattaches to the blunt body, it induces a series of compression waves coalescing into a reattachment ring shock. The counterflow jet interaction replaces the single bow shock over a blunt body by a triple-shock structure.

The shock bifurcation phenomenon was also discovered by the experimental study of the jet spike.[11,12] The counterflow jet of a blunt body in supersonic regime has two distinct states. At the lower injection pressure, the jet displaces the bow shock upstream. The modified shock envelope is generally conical, and the flowfield is unsteady. At higher injection pressures, the displaced shock actually retracts back from the conical to a blunt formation and returns to

---

Received 15 July 2001; revision received 15 November 2002; accepted for publication 15 November 2002.

*Senior Scientist, Center of Excellence for Computing Simulation; currently Research Professor, Mechanical and Materials Engineering, Wright State University, Dayton, OH, 45435. Fellow AIAA.

†Aerospace Engineer, Center of Excellence for Computing Simulation.

‡Assistant Professor, Mechanical and Materials Engineering. Member AIAA.

§Aerospace Engineer, Center of Excellence for Computing Simulation. Member AIAA.

steady state.[11–14] At the bifurcation point between steady and unsteady states, the drag also attains its minimum value. In essence, the bifurcation is the consequence of breakdown of the subsonic feedback loop between the Mach disk and the unstable free shear layer. As the jet injection rate increases, the subsonic region connecting the Mach disk and the free shear layer diminishes in size. At the bifurcation point, a portion of the counterflow, supersonic jet diverts from the Mach disk, effectively cutting off the upstream signal propagation from the free shear layer, then oscillatory motion ceases.[11]

The blunt body in hypersonic, weakly ionized air with an applied magnetic field constitutes the true magnetoaerodynamic phenomenon.[17] In the earlier and the present experiment arrangement, the applied magnetic field is generated by a coaxial pulsed magnet coil in the blunt body. The polarity of the applied magnetic field, thus, is aligned with the axis of the blunt body instead of a transverse field. According to the right-hand rule for applied magnetic field, electrical current, and thrust, the resultant force would not be in the axial direction of the body. Therefore, the drag of the blunt body will remain unaltered. However, a significant change in flowfield structure is anticipated. The present effort attempts to verify this point and to quantify the variation of the bow shock standoff distance in conjunction with the magnetic interaction parameter S.

The present effort consists of two distinct phenomena: the counterflow plasma injection and a magnetoaerodynamic blunt body in hypersonic stream. First, a side-by-side experimental and numerical approach will focus on plasma injection from a hemispherical cylinder at a freestream Mach number of 5.8. Experimental measurements include schlieren photographs, axial aerodynamic force component measurements, and the spectral data of aerodynamic load sensors under the tested conditions. The numerical simulations are generated by solving the axisymmetric, compressible Navier–Stokes equations based on the unstructured grid technique. The calculations are concentrated in the stagnation region, and only turbulent solutions by a one-equation closure model are generated. The detailed flow structure within the displaced shock layer will be delineated by comparing the numerical results with experimental observations. For the magnetoaerodynamic blunt-body hypersonic flow, the weakly ionized air is generated by a dc glow discharge upstream to the bow shock. The applied magnetic field will be produced by a coaxial pulsed magnetic coil embedded in the hemispherical cylinder. The transport property of the generated plasma field and the applied magnetic field will be described in detail.

II. Experimental Facility

The counterflow plasma jet and the blunt body in weakly ionized air are tested in a blowdown, open-jet, high Reynolds number wind tunnel. This wind tunnel was designed to simulate flows at a nominal Mach number of 6.0, at the stagnation temperature of 610 K (1100°R) and a range of stagnation pressures from 3.44×10^2 to 1.38×10^4 kPa (50 to 2000 psi). The mass flow rate of the experiment spans a range from 0.77 to 4.63 kg/s, and this facility can sustain a test period up to 10 min. The blunt-body model is a hemispherical cylinder that has a nose radius and a total length of 38.1 and 203.2 mm (1.5 and 8.0 in.), respectively. The basic models for both the plasma injection and the experiment in weakly ionized air are identical.

The model for plasma injection was fitted with a conical nozzle to accommodate the plasma torch. To be compatible with the energy input to the air supply of the torch, the nozzle was designed with a throat diameter of 1.5 mm. The nozzle has a length-to-diameter ratio of 6.42 and an exit Mach number of 3.28. At the injection stagnation pressure of 482.6 kPa (70 psi) and temperature of 294 K (529°R) respectively, the calculated mass flow rate is 0.52 gm/s (0.0011 lbm/s). For the plasma torch experiment, the stagnation pressure input to the torch has an operational range from 482.6 to 965.3 kPa (70 to 140 psi). The resultant range of mass flow rate is below the critical point of the counterflow jet bifurcation. Therefore, the plasma torch experiments were tested exclusively in the unsteady flow regime.[11,12]

For the present investigation, the tunnel is operated at the lowest freestream density of 0.0118 kg/m^3, which still yields a mass flow rate of 0.77 kg/s and the freestream pressure of 2 torr (0.037 psi). To circumvent the condensation of the air in the test section, the stagnation temperature is maintained at a constant value of 610 K and the static temperature of 79 K (142.2°R) for all cases studied. Under this tested condition, the Reynolds number has a value of 4.52×10^4/m (1.38×10^6/ft). Additional information of the testing environment may be found in Refs. 11 and 12.

Both the plasma injection and the blunt body in an electrically conducting medium require plasma generation. For the magnetoaerodynamic blunt body, the weakly ionized air is produced by a dc glow discharge within the test chamber and upstream of the model. The applied magnetic field is derived from a coaxial pulsed magnet coil built in the blunt body. For the plasma injection, the counterflow ionized air is generated by a plasma torch embedded within the model and issues from the stagnation point. The aerodynamic force is collected by a set of three piezoelectric force sensors or load cells (Fig. 1). The transport properties of the plasma are collected by an emission spectrometer for gas temperature and a double langmuir probe for electron density and electron temperature.

The dc discharge is provided by an Universal Voltronics BRC-10-1000R STD-3PH-208V reversible polarity switching power supply. This power supply unit is rated at 8 kW with 10 kV output source at a signal impedance of $10 \times 10^3\,\Omega$. The maximal current output is limited to 1 A. For plasma generation in the test chamber using the dc supply, a copper ring isolated from the tunnel was used as the anode, and the isolated nose cap of the cylindrical model was connected as the cathode. A single dc power supply unit was sufficient to sustain a stable and diffusive glow discharge at an electrical potential strength of 3000 V. The electrons of the dc plasma generation are obtained from the secondary emission caused by the bombardment of the cathode by positive ions. The ionization is mostly from the outer shell of electrons, the so-called valency electrons. This mode of plasma generation is the most energy efficient. At the relatively low freestream pressure of 2 torr, a uniform glow discharge was achieved until the ambient pressure exceeded the value about 3 torr, then the discharge appeared as a group of steamers.

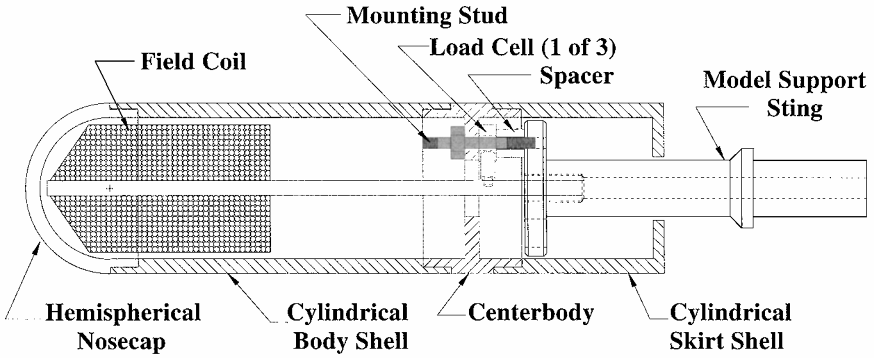

Fig. 1 Force measuring model.

A plasma cutting torch from Thermadyne supplies the ionized air for the counterflow jet. This torch consists of two basic units, the PAK Master 50XL power supply and the PCH/M-28 torch. The maximum power output from this plasma torch is rated at 35 A with an ac input single-phase voltage of 208. However, in the present application, the unit is strictly operating in the starting mode. Therefore, the power output is far below the rated value. The arc starting circuit has a high-frequency generator that produces an ac voltage from 5000 to 10,000 V at a frequency of approximately of 2 MHz. The pilot arc within the torch head is initiated in the gap between the cathode and the positively charged tip. The pilot arc ionizes the compressed air passing through the torch head and exits through a small orifice in the torch tip with a swirling velocity component. The plasma is further expanded by a conical nozzle built in the force measuring model. The plasma jet exits the nozzle at a Mach number of 3.28, if a sonic condition prevails at its throat.

The coaxial, pulse solenoid coil within the model is designed to generate a magnetic field strength up to 2.0 T at the pole. Meanwhile, the calculated maximum pulse discharge current is 920 A and takes 5 ms to exhaust the bank of four capacitors rated at 7700 μF each. Because the magnetic flux density decays rapidly according to the inverse cubic power of distance from the pole, the magnetic flux density at the stagnation point of the blunt body is calculated to be 1.4 T. At the bow shock, the calculated magnetic field intensity along the axis of symmetry is further reduced to a value of 0.75 T. Neodymium rare earth (NeFeB) magnets have also been tested. The maximum flux density at the pole indicates a value of 0.47 T.

The aerodynamic force was measured by load cells and later verified by a strain gauge. For most experiments, three load cells were used to record the total aerodynamic force along the body axis. These load cells, or quartz-force rings (ICP Model 201B03) have a maximum compression range of 11.1 kN and a sensitivity of 44.4 N. The force data were recorded by these cells by a prestressed load of 2.2 kN to operate in the linear measuring range. To minimize the electrical signal interference for the magnetoaerodynamic experiment, the force was record by a strain gauge through a pivot hinge at the base of the model support. Data collected by both measuring devices showed close agreement with each other. By this arrangement, the total axial force exerted on the entire model, includes the wave drag, skin-friction drag, base drag, and the reverse thrust of the counterflow jet.

III. Numerical Analysis

An experimental and computational side-by-side investigation is essential for studying the complex self-sustained fluid motion highlighted by a jet spike shock bifurcation. The detailed dynamic event of the counterflow jet and its associated multiple shock wave structure can only be obtained by solving the time-dependent, axisymmetrical Navier–Stokes equations. The system of governing equations is solved by an implicit, unstructured Euler/Navier–Stokes solver, Cobalt.[15] The numerical algorithm is based on Godunov's Riemann formulation and implicit time stepping to yield second-order spatial and temporal accuracy (see Ref. 16). The numerical procedure is developed for a cell-centered, finite volume approach and able to accommodate a single-grid system that may consist of a variety of cell types, tetrahedron and hexahedron, in three-dimensional space. The neighbor-cell connectivity of a unstructured gird formulation also enhances an exceptionally scalable, parallel computing performance when this numerical procedure is ported to multicomputers using a message passing interface library.[17]

The governing equations are discretized by the fully implicit numerical scheme as

$$[3(U^{n+1} - U^n) - (U^n - U^{n-1})]/2\Delta t + \nabla \cdot F = 0 \qquad (1)$$

where U are the conservative independent variables $U(\rho, \rho u, \rho v, p)$ and F are flux vectors of the Navier–Stokes equations. The reconstruction of the flux vectors at the centroid of the cell faces is by a least-square solution to the approximation

$$U_{i\pm\frac{1}{2}} = U_i \pm \bar{r} \cdot \nabla U_i \qquad (2)$$

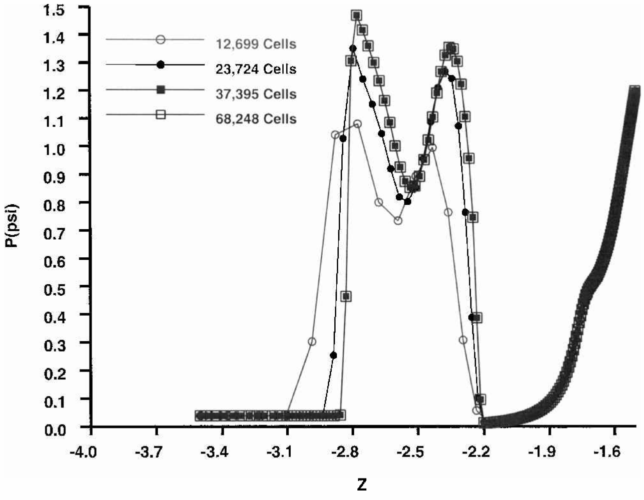

Fig. 2 Grid refinement for shock resolution.

where $U_{i\pm 1/2}$ are the reconstructed left and right sides of the variables at the cell interface and ∇U_i is the gradient vector for the cell i.

In the present application, the no-slip velocity components and adiabatic temperature conditions are imposed on the blunt-body surface. For the plasma torch, the sonic throat is prescribed at the entrance boundary for the conical nozzles. The unperturbed freestream condition is specified at the upstream boundary and the no-reflection condition downstream for the far field. Turbulent closure is achieved by the Spalart–Allmaras one-equation model.[18]

The numerical accuracy is assessed by generating four consecutive solutions on increasingly refined grids. For the shock-dominant problem, the error criterion for evaluation is the shock definition and the standoff distance. At a freestream Mach number of 5.8 and a Reynolds number based on nose diameter of 3.45792×10^5, the axisymmetrical flowfield around the hemispherical cylinder is calculated on four different grid systems that consist of 12,699, 23,724, 37,395, and 68,248 cells.

In Fig. 2, the pressure distributions are presented along the axis of symmetry from the undisturbed freestream toward the blunt body. These pressure distributions reveal the rapid compression and expansion process at the bow shock and the forward motion terminating Mach disk. The pressure distribution also shows the final and continuous expansion from the counterflow jet exit into the shock layer. The numerical results are essentially grid independent after the third grid refinement. The calculated and measured standoff distances compare very well with the correlated data by Ambrosio and Wortman.[19] The normalized values by the nose radius are $\Delta/r = 0.155$ and 0.157, respectively. For the finest mesh system, the average law-of-the-wall variable y^+ is around unity. The finest grid distribution is adopted for the rest of the present computations.

IV. Accuracy Assessment

The uncertainty in experimental data arises mostly from the drag measurement using load cells. these piezoelectric quartz sensors have built-in microelectronic amplifiers, which convert the high-impedance electrostatic charge from the crystals into a low-impedance voltage output. Therefore, it is most effective for measurement of a dynamic event. In the present investigation, the testing sequence is designed to take advantage of this feature. Efforts have been made to maintain an isolated environment for the sensors from electromagnetic and thermal interferences. From the seven sets of data, including two data sweeps and four discrete measurements, the data scattering band is less than 1.7%. However, the major portion of the data discrepancy between sweeps is in the determination of the absolute drag value after the model is injected in the tunnel jet stream. The overall measurement uncertainty is around 7%.

Another source of the experimental uncertainty is the thermodynamic state and transport property of the plasma. Although the internal energy partition among different quanta of the vibrionic mode is uncertain, the average vibrionic temperature of the plasma is determined to be 4400 ± 400 K. It is arguable that the internal degrees of freedom of translation, rotation, and vibration are in thermal equilibrium. The electron temperature obtained from the langmuir probe near the sonic region in the shock layer was around 20,000 K. The corresponding electron density, which is highly dependent on the location relative to the plasma plume yielded a value of $3 \times 10^{12}/\mathrm{cm}^3$ or higher. When the chemical composition for the equilibrium state is assessed, it is unrealistic to assume the plasma torch is in a state of thermodynamic equilibrium.[11,12] Nevertheless, the nonequilibrium chemical kinetic effects on the flow may still be small in view of the extremely low concentration of ionized components in the plasma jet.[5,6]

The numerical error of the present results consist of two elements, the inappropriate governing equations and computational accuracy. The error that incurred by solving overly simplified governing equations for magnetoaerodynamic phenomena presently cannot be assessed. For the present numerical simulations, neither the chemical kinetics nor the finite electrical conductivity electromagnetic effects have been taken into consideration to reflect the state-of-the-art development.[6]

For a shock-dominant problem, the criterion of numerical error evaluation is the shock definition and its standoff distance. In essence, the captured shock region is only first-order accurate for all approximate Riemann formulations. The computational error is assessed by generating solutions on consecutively refined grids immediately adjacent to the shock. The grid refinement was focused on the anticipated bow shock location. The calculated shock standoff distances, defined by the sonic point of the captured shock, were essentially grid independent after the third grid refinement. The identical process was also applied to nozzle configurations of smaller throat diameter nozzles.

V. Transport Property of Plasma Torch

Initially, the rotational temperature of air plasma was attempted by the optical emission from the second positive electronic transition $C^3\Pi_u \rightleftharpoons B^3\Pi_g$ of molecular nitrogen.[20–22] However, the nitrogen C–B spectra were obscured by emission from other species, such as the molecular oxygen and nitric oxide, as well as vapors of copper and iron. Nevertheless, the origin band (0, 0) of the ionized nitrogen N_2^+, $C^2\Pi_u^+ \rightleftharpoons X^2\Pi_g^+$ appears as a prominent feature in the plasma torch emission spectrum. A composite spectrum of the plasma torch in the 3400–4400 Å wavelength range was obtainable.[20,22] The average vibrionic temperature, determined from the Boltzmann plot and a blackbody modeling is 4400 ± 400 K (7920 ± 720°R).

The electron density and temperature of the plasma field around the torch and the magnetoaerodynamic experiment of the blunt body are measured by a double langmuir probe (See Refs. 23 and 24). The probe is constructed from 0.5-mm platinum wire. The electrical potential is provided by a ±100 V Kepco bipolar power supply. To determine the entire current–voltage characteristic, electrical current measurement capability in the microampere range is essential. For that purpose, the resistor in the circuit can vary from 1030 to 11,305 Ω (Ref. 24). The langmuir probe has a double-hole ceramic sleeve and a wire separation distance of 1.0 mm, and the sensing area of each probe is 2.1 mm^2. Although the platinum wire has a high resistance to oxidation at high temperature, the langmuir probe is still limited to the fringe area away from the plasma plume.

For the plasma injection, a langmuir probe survey of the entire shock layer was carried out at the lowest plasma injection pressure 482.6 kPa (70 psi). Two different survey mechanisms were used. Close to the centerline of the plasma plume, the probe is introduced from the nose cap of the blunt body. Downstream from the nose cap, the survey was conduced by a traverse mechanism mounted on the top wall of the test chamber. The closest survey radial distance from the centerline of the plasma plume without thermally shattering the probe is 0.76 cm (0.3 in.). Based on numerical results, the local temperature is around 3600 K (2000°R) (Ref. 12). The data were sampled from a distance as close as 0.1 cm from the nose cap to beyond the deattached bow shock. In general, the electron number density, electrical conductivity, electron temperature, and electrical field strength attain the maximum value in the plasma plume. The magnitude of these plasma transport properties within the shock layer decreases toward downstream. Because the flowfield is in the subcritical state of shock bifurcation, the measurements exhibit a very wide scattering band. The data scattering also decay rapidly from the plasma plume and then slowly dissipate downstream. The plasma field over the hemispherical nose region is given in Fig. 3.

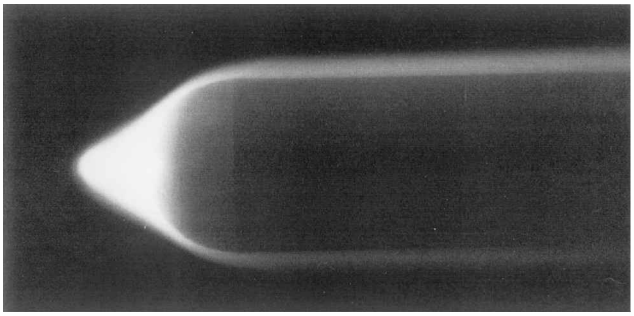

Fig. 3 Total field of plasma injection.

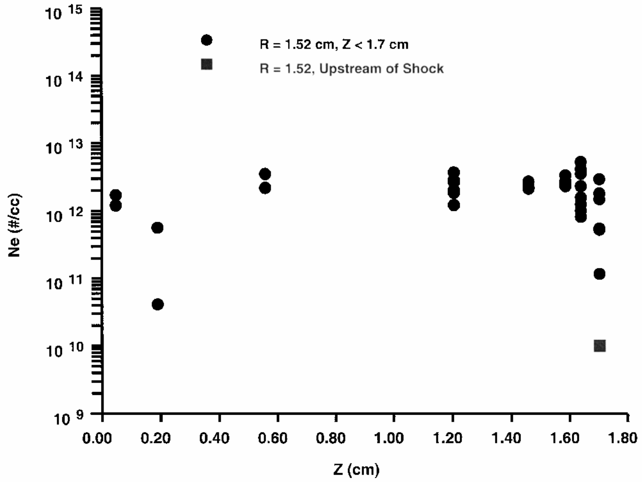

Fig. 4 Electron number density distribution, $r = 1.52$ cm.

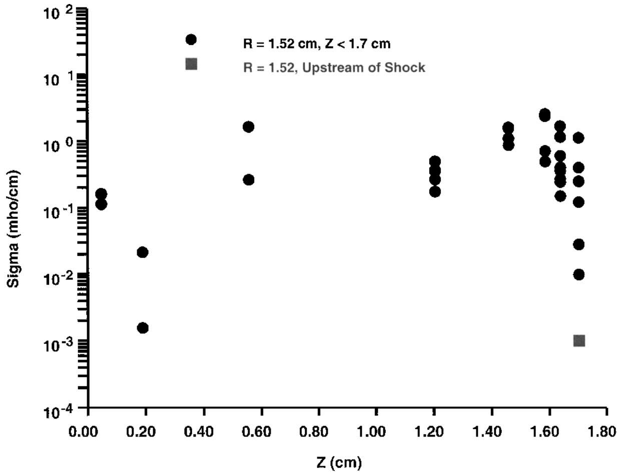

Fig. 5 Electrical conductivity distribution, $r = 1.52$ cm.

Typical electron number density, electrical conductivity, and electron temperature distributions are presented in Figs. 4–6. These data are collected along a constant radial distance, $r = 1.52$ cm, from the blunt body to beyond the enveloping bow shock. In Fig. 4, the electron number density distribution across the shock layer is shown. The measured number density of electrons fluctuates around the value of $2 \times 10^{12}/\mathrm{cm}^3$. The number density increases slightly approaching

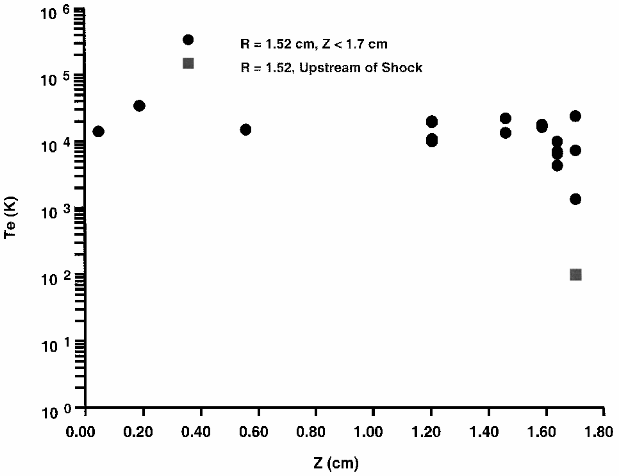

Fig. 6 Electron temperature distribution, $r = 1.52$ cm.

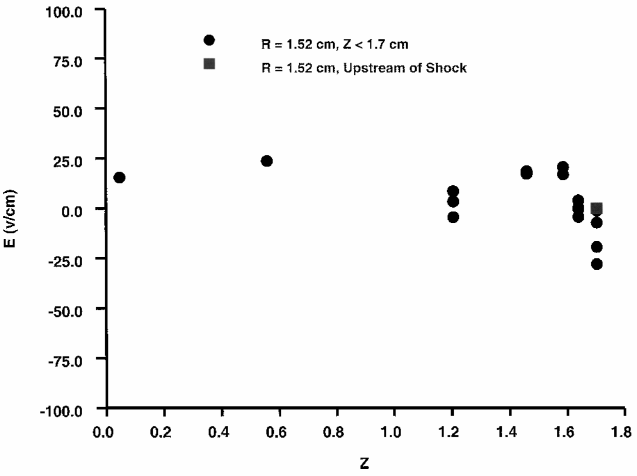

Fig. 7 Electrical potential distribution, $r = 1.52$ cm.

the bow shock then drops drastically across the shock. In this aspect, the shock wave is acting like a barrier in preventing heavy charged particles to escape the shock envelope. One would expect that charge separation takes place across the shock front like that of the region of electrodes. However, the present measurement does not have sufficient resolution to draw a definitive conclusion. The electrical conductivity distribution along the same trace exhibits the nearly identical behavior as that of the electron number density in Fig. 5. This behavior is anticipated because the electrical conductivity σ is linearly proportional to the electron number density and electron mobility.[23,24] For the present experiment, the electrical conductivity yields an average value 60 mho/m across the major portion of the shock layer, rises to a slightly higher value of 140 mho/m at the shock, and falls to a very low and unmeasurable value upstream of the shock.

The electron temperature distribution of plasma in the shock layer is presented in Fig. 6. The statistical average value across the shock layer in the constant radial array is 20,000 K (36,000°R). Beyond the bow shock envelope, the electron temperature of the plasma falls below the value that can be measured with any certainty. In spite of the extremely low concentration of ions such as NO^+, O_2^+, and N_2^+, this measurement clearly shows that the plasma field is not in the state of thermal equilibrium. Finally, the electrical potential of the plasma torch along the same constant radial array is shown in Fig. 7, and the overall measured potential is confined with ±30 V/cm. At the shock front, the electrical potential reveals predominant negative values in contrast to the rest field within the shock layer. It may be viewed as an additional evidence of charge separation.

To differentiate the electromagnetic effect from the aerodynamic interaction and thermal phenomenon, an applied magnetic field is imposed on the plasma stream. A set of NeFeB magnet collars have been placed around the counterflow nozzle, and the maximum magnetic flux density at the pole registers a value of 0.47 T. The magnetic field is aligned with the axis of the nozzle. The polarity of the magnet is also reversed to seek a possible change in drag. Thus, the applied magnetic field is expected to produce a difference in total drag.

VI. Plasma Injection Experiment

In the plasma injection experiment, the plasma is generated by a plasma cutting torch embedded in the force measuring model. Because the power output of the torch in the startup mode is rather limited, only a small amount of air supply can be ionized. In the experiment, the stagnation pressure of the air supply spans a narrow range from 482.6 to 965.3 kPa (70 to 140 psi). In this counterflow jet stagnation pressure range, the flow is in the subcritical bifurcation state and is characterized by unsteadiness.

At the plasma temperature around 4400 K (7920°R) and maximum static pressure within the shock layer of 10.5 kPa (78.9 torr), the plasma chemical composition in equilibrium condition can be determined from numerous databases.[25] The mass fractions of molecular nitrogen and nitric oxide are 0.68 and 0.05, respectively. The oxygen molecules are nearly all dissociated to yield a mass fraction of atomic oxygen around 0.26. The components of N^+, NO^+, N_2^+, and O^+ are on the order of magnitude from 10^{-5} to 10^{-10}. These low mass fractions are essentially considered trace elements, but in these highly excited states, these chemical species can still have a significant amount of energy content. Although the plasma counterflow jet is understood to be in a thermodynamically nonequilibrium state, the chemical composition and internal energy partition can not be predicted with certainty. To avoid this uncertainty, the fluid dynamic behavior of the aerodynamic interaction is evaluated by the mass-averaged, time-dependent, axisymmetric Navier–Stokes equations without the detailed chemical kinetics but with equilibrium air composition. However, it is reasonable to assume that the vibrionic temperature (4400 ± 400 K) is in thermal equilibrium with the translational and rotational degrees of freedom but not necessarily with electron temperature ($T_e = 20{,}000$ K) (Refs. 3 and 5). In short, the temperatures of the injected plasma are comparable to that reported by Ganiev et al.[10]

The composite schlieren photograph at four different stagnation pressures of the plasma injection is presented in Fig. 8. The plasma is injected into the bow shock envelope at stagnation pressures of 582, 689, 827, and 965 kPa (70, 100, 120, and 140 psi). Two major features of the plasma injection in contrast to the room temperature counterflow jet stand out. First, the shock waves uniformly retract toward the blunt body for all cases tested. Based on the perfect-gas model calculation, this phenomenon is mostly associated with a reduced mass flow rate by the elevated plasma temperature.[11,12] The mass flow rate of the nozzle is linearly proportional to the stagnation pressure and inversely proportional to the square root of the stagnation temperature $\dot{m} \sim (p_0/\sqrt{T_0})_j$. Under the present testing condition, the mass flow rate is reduced by a factor of 3.9.

The other feature of plasma injection is that the amplitude of the unsteady shock wave movement is significantly subdued. However, the basic oscillatory behavior between two different injectants is similar, and the most predominant oscillatory mode occurs at 100 Hz. Over the frequency range from 500 to 2500 Hz, the oscillatory amplitude of the plasma injection is roughly 10 dB lower than the room-temperature air counterpart. This behavior is dramatic on the video recording, and the same observation can also be made from the blurred photographic images of the room-temperature injection of the sharply defined shock structure by the plasma injection. At the lowest plasma injection pressure [482 kPa (70 psi)], two biased bow shocks appear to dominate over others, but the unsteady movement of shock waves persisted. These two contrasting features between the room-temperature air and plasma injection are uniformly observed over the entire tested pressure range.

The side-by-side comparison of schlieren photographs and computed results of the counterflow plasma injection is given in Fig. 9. For the comparison case, the stagnation pressure of the jet is 482.6 kPa (70 psi), and the ratio of the stagnation pressures of the jet and the tunnel is 1.4. The injecting rates are 0.52 and 0.13 g/s at the stagnation temperatures of 294 K (530°R) and 4400 K (7920°R), respectively. The plasma jet computation is based on the assumptions that the sonic condition prevails at the nozzle throat and that the chemical composition of the plasma is not drastically different from the equilibrium condition. Therefore, the thermodynamic properties of the plasma can be approximated by the equilibrium air composition. Because the unsteady flowfield is induced by a feedback mechanism associated with free shear layers, numerical results using turbulent closure are unable to resolve the physical phenomena in this fine scale. In essence, the experimental observed bistable state of the shock structure is not resolved by the present numerical simulation. Nevertheless, the essential affinity of schlieren photographs obtained by experiment and the calculation is reasonable.

VII. Results of Plasma Injection

The drag data at four tested stagnation pressures of the plasma counterflow jet and the computed results are presented in Fig. 10. The discrete data set is accompanied by results from room-temperature air injection in a single data sweep. These continuous data distributions serve as a reference for individual drag measurements. The agreement between measurements and calculations at the low-temperature injection is about 5%, the same magnitude as the data scattering band. In the present data collection process, the drag measuring procedure starts with room-temperature air injection. The plasma is then introduced by igniting the torch and is sustained for a duration of 15 s. The piezoelectric force sensors have yielded consistent output immediately after the transient electromagnetic pulse has subsided. The individual drag measurement of the room-temperature air injection registers a value close to the values from the data sweep. The measured drags rise when the plasma is ignited. According to the present and previous computational analyses of comparable simulations, this behavior is mostly due to reduced mass injection flow rate.[11,12] There is little doubt that the plasma injection has produced a greater drag reduction than the room-temperature air injection at the identical mass flow rate. However, it is not completely certain that all of the additional drag reduction is derived from thermal energy deposition.

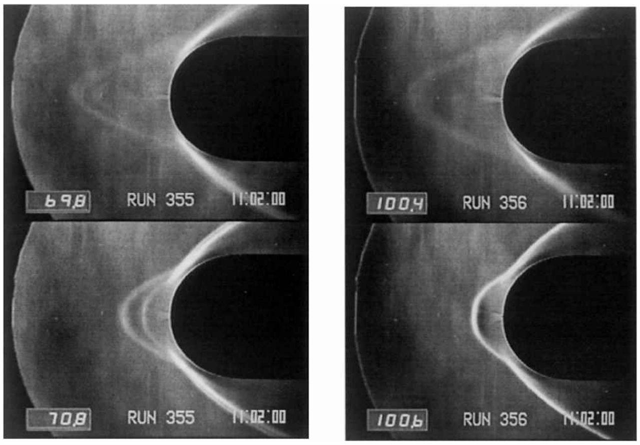

a) $P_j = 582$ **kPa (70 psi)**

b) $P_j = 689$ **kPa (100 psi)**

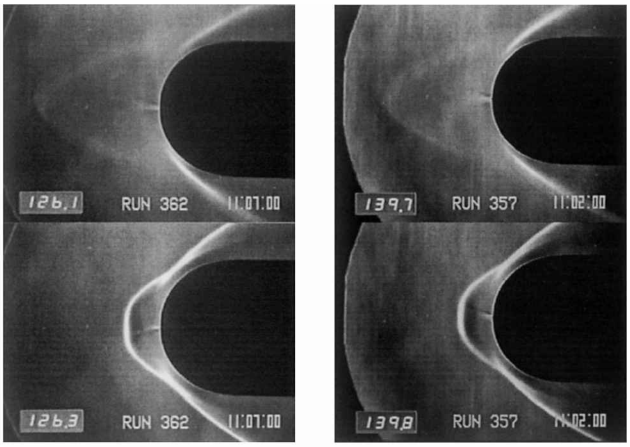

c) $P_j = 827$ **kPa (120 psi)**

d) $P_j = 965$ **kPa (140 psi)**

Fig. 8 Schlieren photographs of plasma injection.

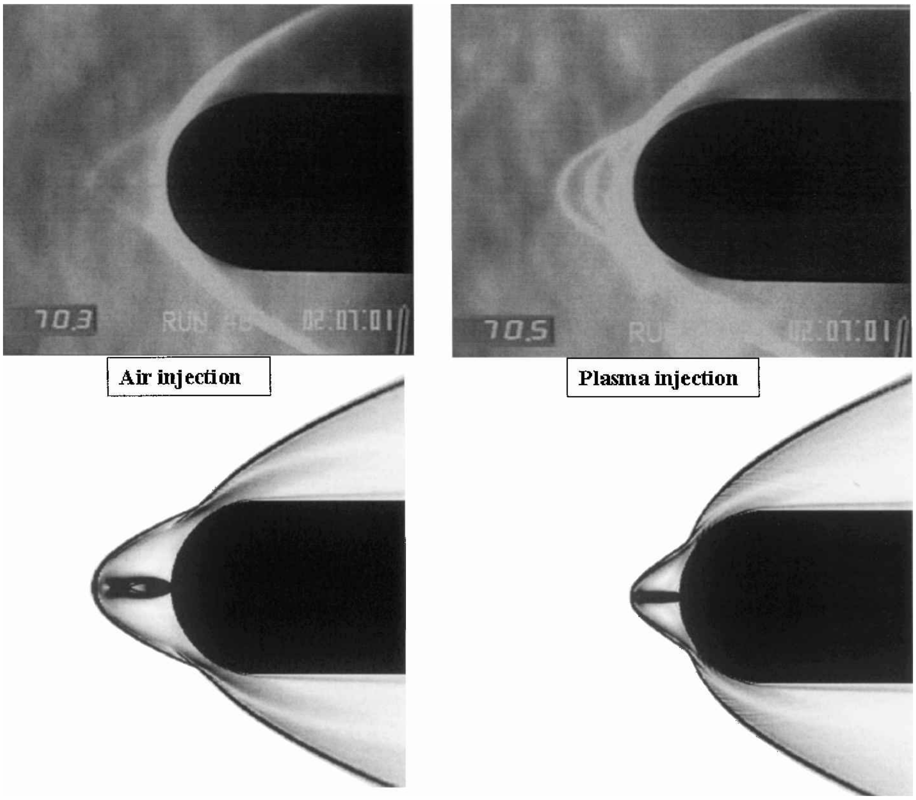

Fig. 9 Comparison of schlieren and computation.

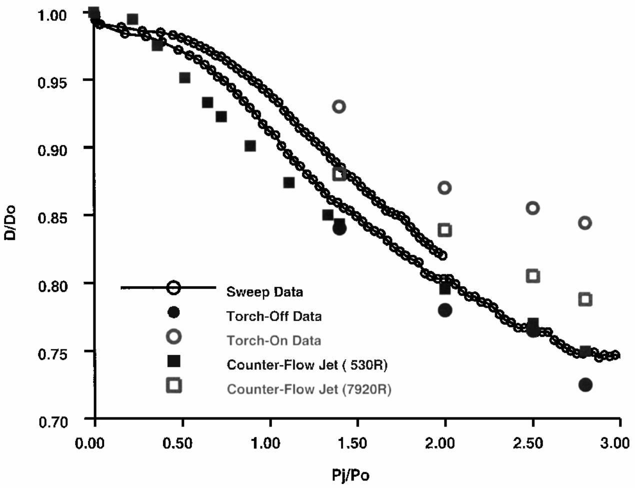

Fig. 10 Drag data vs plasma injection pressure.

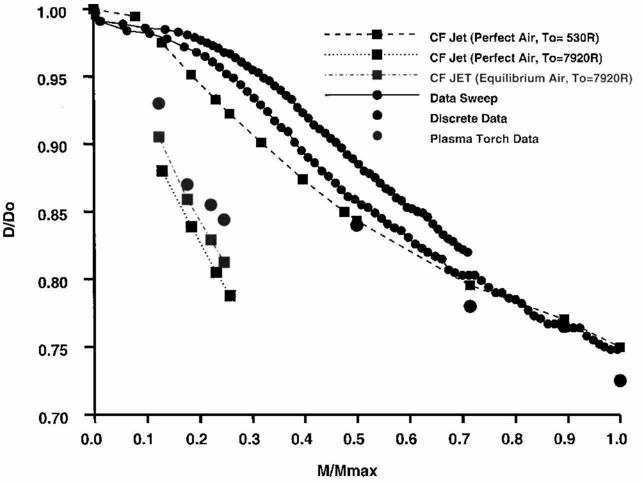

Fig. 11 Drag data vs injecting mass flow rate.

The controlling parameters of the counterflow jet are the jet mass flow rate, jet exit Mach number, and thermodynamic property of the injectant.[11–14] In the present effort, the jet exit Mach number is 3.26. For plasma injection, the nonequilibrium weakly ionized air not only changes the temperature but also the thermodynamic property of the injectant. At present, an accurate description of the nonequilibrium plasma is far from ascertained, but a reasonable measurement of injectant temperature is possible by emission spectra. Therefore, only the thermal effect on plasma injection rate can be isolated and is analyzed by solving the mass-averaged Navier–Stokes equations with a known equilibrium air composition.

The equilibrium chemical composition of the plasma counterflow jet can be obtained in terms of mass fraction at the thermodynamic state near the Mach disk in the shock layer (4400 K and 10.5 kPa). The mass flow rates of the plasma counterflow jet were calculated by solving the Reynolds averaged Navier–Stokes equations based on the equilibrium composition. The computed mass flow rate yields values of 0.13, 0.19, 0.23, and 0.26 g/s, which corresponds to the nominal injection pressure ratios p_j/p_0 of 1.4, 2.0, 2.5, and 2.8, respectively. The drag data are presented in Fig. 11, as a function of the mass flow rate. In this physically meaningful format, the drag reduction by plasma injection can be easily explained. The calculated mass flow rate at the higher stagnation temperature of 4400 K (7920°R) reveals that, at the identical mass flow rate, the plasma injection indeed produces a greater drag reduction than its room-temperature counterpart. However, the major portion of the reduced drag is derived from the thermal deposition of the plasma. However, when energy is distributed among different internal degrees of excitation, the drag reduction diminishes. Under this condition, the difference between calculated results and measurements is confined within the band of data uncertainty.

In an attempt to further define the electromagnetic effect for the plasma counterflow jet, an applied magnetic field was imposed by a set of NeFeB magnets around the plasma torch chamber. The applied magnetic field is aligned with the axis of the nozzle to enhance the plasma pinch effect.[23] The magnet has a maximum magnetic flux density of 0.47 T at the pole, but the field strength diminishes rapidly toward the nozzle axis. The estimated value is about 0.17 T locally, and the plasma interaction parameter $S = (\sigma B^2 R/\rho u)$ is uncertain but much less than unity. Under this circumstance, the effects of electromagnetism are difficult to detect. As anticipated, only limited success was achieved at the lowest plasma stagnation pressure. The difference between plasma and room-temperature air injection including the applied magnetic field is detectable but is confined within the uncertain data scattering band.

The electromagnetic force of the plasma injection may also enter the interaction mostly through conductive current and transport of excess charges.[23] Significant charge separation may occur at locations where the disparity of electron and ion mobility are accentuated, such as near the electrodes and across the shock wave. Because an electromagnetic field modifies the Rankine–Hugoniot condition across a shock (see Refs. 2 and 3), the charge separation at the shock wave is one of the likely sources to affect the wave drag. Unfortunately, the present measurements by the double langmuir probe lacks the resolution to be conclusive.

VIII. Electromagnetic Fields Generation

The magnetoaerodynamic experiment is designed to be parallel to that of Ziemer.[7] However, there is a critical difference between experiments in the plasma generating process. In the present experiment, the weakly ionized air is generated by the dc glow discharge and the effect of nonequilibrium chemical kinetics may become negligible. In the present setup, the nose cap serves as the cathode, and a copper ring that grounds to the metal frame of wind tunnel is used as the anode. The shortest streamwise distance between the electrodes is 5.0 cm. When the plasma is ignited at the freestream pressure of 2 torr, the glow discharge can be easily maintained by an electrical potential of 3000 V and a current up to 800 mA with a power of 2.4 kW.

The entire plasma field is presented in Fig. 12. The surface glow of the nose cap is concentrated mostly at the juncture of the hemispheric nose and the cylindrical afterbody, which indicates the weakly ionized air upstream to the model is nonuniform. The concentration of the surface glow at this location is enhanced by both the sharp juncture edge of the nose cap and a lower local static pressure after a rapid expansion from the stagnation point. The pressure and temperature at the stagnation point of the blunt body is 78.7 torr (1.52 psi) and 592.0 K (1064.8°R), respectively. It is well known that the breakdown of the glow discharge around the electrode is most sensitive

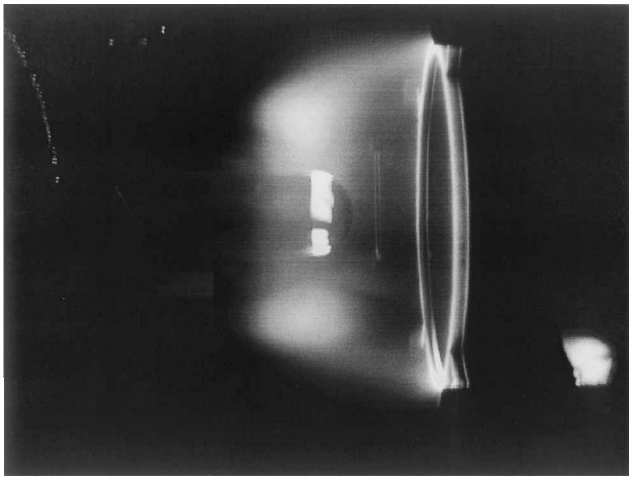

Fig. 12 Plasma field of magnetoaerodynamic experiment.

to the ambient pressure.[23] The uniform and diffusive plasma field degenerates into arc streaks when the static pressure in the tunnel increases from 2 to 3 torr. This behavior was also noted in the earlier experiment conducted in a vacuum chamber.[5]

From the langmuir probe survey, the typical plasma field upstream of the bow shock can be characterized to have an electron number density of 2–10 × 10^{12}/cm^3, an electrical conductivity of 7–30 mho/m, an electron temperature about 160,000 K, and the electrical field strength up to ±60 V/cm. The distribution of the electrical conductivity along a constant radial distance from the body axis, $r = 6.35$ cm, is shown in Fig. 13. The streamwise distance Z is now measured from the stagnation point toward downstream. The rapid rise of measured values at $z \geq 3.8$ cm within the shock layer may be attributable by probe interference near the electrode. This low electrical conductivity of the glow discharge may be understood from the low mass fraction of the ionized air components. The dc glow discharge supplies merely 2.4 kW to the tunnel stream with a high mass flow rate of 0.77 kg/s. This miniscule energy input from the dc discharge is unlikely to significantly alter the thermodynamic state of the airstream in comparison with the 950 kW of power input from multistage compressors and the pebble bed heater. As a reference point of the testing environment, the electrical conductivity of Ziemer's experiment in an electromagnetic shock tube ($2800 \leq \sigma \leq 5500$ mho/m) is nearly two orders of magnitude greater than the present condition.[7]

The key element of a magnetoaerodynamic phenomenon is the presence of an applied magnetic field. The modification to the Rankine–Hugoniot condition is most effective through a transverse field with respect to the electrical current (see Refs. 2–5). In the present test, the applied magnetic field is aligned with the body axis. Several applied magnetic fields were attempted including a low-current solenoid with steel core concentrator, NeFeB magnets, and a high-current impulse solenoid. From Fig. 14, the impulse solenoid exhibits the greatest magnetic field strength of more than 1.37 T at the stagnation point. Observe that the magnetic field strength decays rapidly toward the bow shock and that the strength is reduced to less than 0.75 T locally. The pulse current is delivered from a bank of four capacitors (7700 μF each) with a peak current of 920 A. The bank of capacitors can sustain discharging current greater than 850 A for a duration about 5000 μs. From Zeimer's experience (a total of 35 μs), this time frame will be sufficient for the flowfield to adjust to the electromagnetic effect.[7]

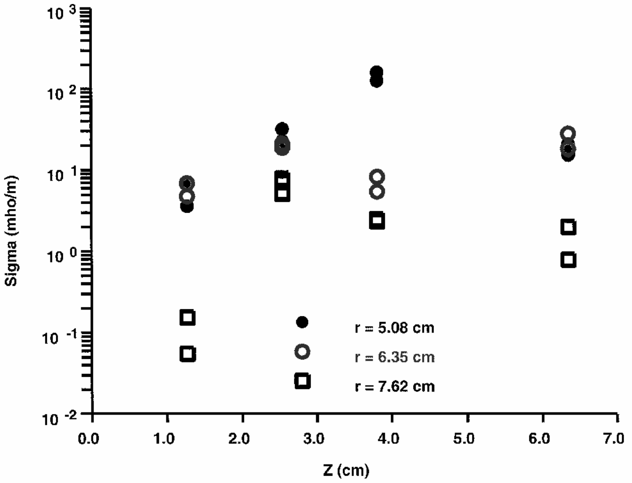

Fig. 13 Electrical conductivity distribution of blunt-body plasma field.

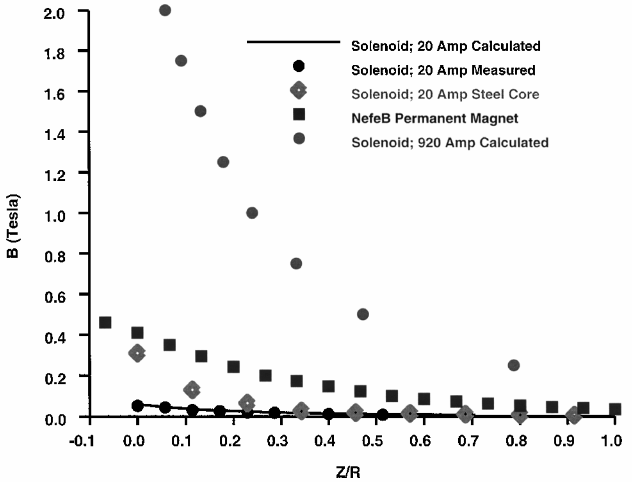

Fig. 14 Applied magnetic field strength along stagnation streamline.

IX. Magnetoaerodynamic Experiment

The procedure for the magnetoaerodynamic experiment is very straightforward. The force measuring model is injected into the tunnel stream when the static pressure reaches 2 torr ($p = 0.04$ psi) and $T_\infty = 79$ k (142.3°R). Then the plasma is ignited and maintained by a steady electrical current up to 920 mA between electrodes. Finally, a trigger switch initiates the discharge of the capacitors bank through the impulse solenoid. The axial force data of the blunt body and schlieren images are collected over a period of 5 ms. The time elapse allows a high-speed video system to capture about five images. This recording period is synchronized with the time frame that the solenoid is energized by an electrical current greater than 850 A.

Under the typical testing condition, the interaction parameter indicates a range of $0.140 \leq S \leq 0.28$, which is far below the value obtained by Ziemer.[7] The requirements to increase the magnitude of the interaction parameter of the present experiment must be concentrated on decreasing the flow density and increasing the electrical conductivity of the plasma and the applied magnetic field strength. For a fixed applied magnetic field strength, the distance or the gap between the solenoid and the bow shock must be significantly reduced. In any event, an instantaneous carbunclelike structure of the bow shock has repetitively appeared (Fig. 15) instead of a uniformly outward displacement of the bow shock detected by Ziemer using an overexposure approach.[7] This anomaly has been observed repeatedly in experiments and appeared as a transient phenomenon from an electrostatic discharge. Partial supporting evidence is that these schlieren images were captured only by a single frame of a 1000-frame/s video system.

The force measuring strain gauge for the magnetoaerodynamic experiment is located at the base of the model support to minimize the electromagnetic interference. The strain gauge has also been carefully calibrated. At the tunnel in-flow condition, the strain gauge gives a total drag of 31.14 N (7 lbf), which is also verified by the computational results. However, when the applied magnetic and plasma fields exist simultaneously, the strain gauge registered a strong pulsing signal. The electrical pulse exists for a period of 1000 μs, which is partially coincided with the duration of the strongest applied magnetic field. From the high-speed video system, the plasma field is observed to be profoundly effected by the applied magnetic field. This behavior is vastly different when the solenoid is energized in the absence of the flowfield in that the strain gauge registers a

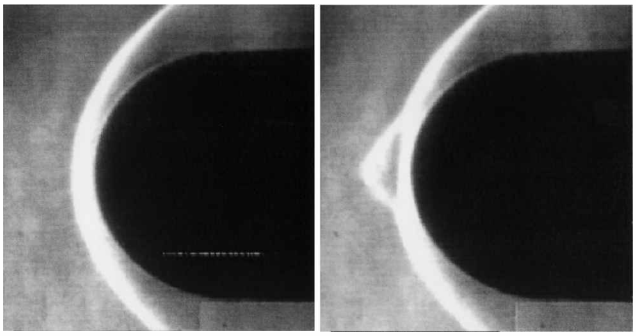

Fig. 15 Modified shock structure by magnetoaerodynamic force.

small-amplitude perturbation and followed by a ringing pattern in the evacuated tunnel [$p = 8.27$ torr (0.16 psi)].

From the present effort, it is unmistakably clear that further magnetoaerodynamic experiments are still urgently needed to establish a solid frame of reference for this interdisciplinary research. The modified Mach 6 tunnel has served its purpose well in guiding future research, as well as opening a new avenue for better understanding of this complex yet promising new technological challenge. However, the need of a specifically designed facility is now critical to explore and to establish a largely uncertain scientific discipline.

X. Conclusions

The drag reduction by a plasma counterflow jet is investigated in a Mach 6 wind tunnel at a freestream pressure of 268.7 Pa (0.040 psi) and temperature of 79 K (142.3°R). The plasma with a vibrionic temperature of 4400 ± 400 K, an electron temperature about 20,000 K, and an electron density greater than $3 \times 10^{12}/\text{cm}^3$ is injected from a hemispherical cylinder. At a given injecting stagnation pressure, the measured drag is nearly 10% higher than the room-temperature air injection. However, if the decreased injection mass flow by the elevated plasma temperature is taken into consideration, the drag reduction by plasma injection is in fact greater than the room-temperature counterpart.

Based on the equilibrium chemical composition at the plasma condition and at the identical injecting mass flow rate, the plasma injection would yield a 12.5% greater drag reduction by the plasma thermal effect alone. The present side-by-side experimental and computational research indicates that the major portions of drag reduction by plasma injection are derived from the favorable shock and counterflow jet interaction and thermal energy deposition. The contribution from the electromagnetism is small and unmeasurable in the present investigation.

The magnetoaerodynamic experiments in a modified conventional hypersonic facility with introduced plasma generator has revealed that a significant and applicable electromagnetic effect must be derived from an appropriate applied magnetic field. It is just a reaffirmation of the pioneering theoretical observations.

Acknowledgments

The computing resource was supported by a Grant from the Department of Defense High Performance Computing Shared Resource Center at Wright–Patterson Air Force Base. The research team deeply appreciates the sponsorship by Steven Walker of the Air Force Office of Scientific Research. The invaluable contributions by James M. Williamson, Dean Emmer, and the wind-tunnel crew, Tom Norris, Ray Raber, and Michael Greene, are duly acknowledged.

References

[1] Resler, E. L., and Sears, W. R., "The Prospects for Magneto-aerodynamics," *Journal Aeronautic Sciences*, Vol. 25, 1958, pp. 235–245, 258.

[2] Sutton, G. W., and Sherman, A., *Engineering Magnetohydrodynamics*, McGraw–Hill, New York, 1965, pp. 295–308.

[3] Mitchner, M., and Kruger, C. H., *Partially Ionized Gases*, Wiley, New York, 1973, pp. 163–241.

[4] Shang, J. S., "An Outlook of CEM Multidisciplinary Applications," AIAA Paper 99-0336, Jan. 1999.

[5] Shang, J. S., Ganguly, B., Umstattd, R., Hayes, J., Arman, J., and Bletzinger, P., "Developing a Facility for Magneto-Aerodynamic Experiments," *Journal of Aircraft*, Vol. 17, No. 6, 2000, pp. 1065–1072.

[6] Shang, J. S., "Recent Research in Magneto-Aerodynamics," *Progress in Aerospace Sciences*, Vol. 37, 2001, pp. 1–20.

[7] Ziemer, R. W., "Experimental Investigation in Magneto-Aerodynamics," *ARS Journal*, Vol. 19, Sept. 1959, pp. 642–647.

[8] Bush, W. B., "Magnetohydrodynamics-Hypersonic Flow Past a Blunt Body," *Journal Aeronautic Sciences*, Vol. 25, Nov. 1958, pp. 685–690, 728.

[9] Meyer, R. C., "On Reducing Aerodynamic Heat-Transfer Rates by Magnetohydrodynamic Techniques," *Journal of the Aero/Space Sciences*, Vol. 25, No. 9, 1958, pp. 561–566, 572.

[10] Ganiev, Y. C., Gordeev, V. P., Krasilnikov, A. V., Lagutin, V. I., Otmennikov, V. N., and Panasenko, A. V., "Aerodynamic Drag Reduction by Plasma and Hot-Gas Injection," *Journal of Thermophysics and Heat Transfer*, Vol. 14, No. 1, 2000, pp. 10–17.

[11] Shang, J. S., Hayes, J., Wurtzler, K., and Strang, W., "Jet-Spike Bifurcation in High-Speed Flows," *AIAA Journal*, Vol. 39, No. 6, 2001, pp. 1159–1165.

[12] Shang, J. S., Hayes, J., and Menart, J., "Hypersonic Flow over a Blunt Body with Plasma Injection," *Journal of Spacecraft and Rockets*, Vol. 35, No. 3, 2002, pp. 367–375.

[13] Finley, P. J., "The Flow of a Jet from a Body Opposing a Supersonic Free Stream," *Journal of Fluid Mechanics*, Vol. 26, Pt. 2, 1966, pp. 337–368.

[14] Barber, E. A., Jr., "An Experimental Investigation of Stagnation-Point Injection," *Journal of Spacecraft*, Vol. 2, Sept.–Oct. 1965, pp. 770–774.

[15] Strang, W. Z., Tomaro, R. F., and Grismer, "The Defining Methods of Cobalt$_{60}$: A Parallel, Implicit, Unstructured Euler/Navier–Stokes Flow Solver," AIAA Paper 99-0786, Jan. 1999.

[16] Tomaro, R. F., Strang, W. Z., and Sankar, L. N., "An Implicit Algorithm for Solving Time Dependent Flows on Unstructured Grids," AIAA Paper 97-0333, Jan. 1997.

[17] Grismer, M. J., Strang, W. Z., Tomaro, R. F., and Witzman, F. C., "Cobalt: A Parallel, Implicit, Unstructured Euler/Navier–Stokes Slover," *Advances in Engineering Software*, Vol. 29, April–July, 1998, pp. 365–373.

[18] Spalart, P. R., and Allmaras, S. R., "A One-Equation Turbulence Model for Aerodynamic Flows," AIAA Paper 92-0439, Jan. 1992.

[19] Ambrosio, A., and Wortman, A., "Stagnation Point Shock Detachment Distance for Flow Around Spheres and Cylinder," *ARS Journal*, Vol. 32, No. 2, 1962, p. 281.

[20] Gilmore, F. R., Laher, R. R., and Espy, P. J., "Franck–Condon Factors, r-Centroids, Electronic Transition, Moments, and Einstein Coefficients for Many Nitrogen and Oxygen Band Systems," *Journal of Physical and Chemical Reference Data*, Vol. 21, No. 5, 1992, pp. 1005–1107.

[21] Herzberg, G., *Molecular Spectra and Molecular Structure. I. Spectra of Diatomic Molecules*, 2nd ed., Van Nostrand, New York, 1950.

[22] Huber, K. P., and Herzberg, G., *Molecular Spectra and Molecular Structure, Vol. IV: Constants of Diatomic Molecules*, Van Nostrand Reinhold, New York, 1979.

[23] Howatson, A. M., *Introduction to Gas Discharges*, 2nd ed., Pergamon, Oxford, 1975, pp. 168–190.

[24] Menart, J., Shang, J. S., and Hayes, J., "Development of a Langmuir Probe for Diagnostic Technique for Plasma Diagnostic Work in High Speed Flow," AIAA Paper 2001-2804, June 2001.

[25] McBride, B. J., and Gordon, S., "Computer Program for Calculation of Complex Chemical Equilibrium Compositions and Applications, II. User Manual and Program Description," NASA RP 1331, June 1996.